Oceanic Overturning and Heat Transport: The Role of Background Diffusivity

MAGNUS HIERONYMUS

Department of Meteorology, Stockholm University, Stockholm, and Swedish Meteorological and Hydrological Institute, Norrköping, Sweden

JONAS NYCANDER, JOHAN NILSSON, AND KRISTOFER DÖÖS

Department of Meteorology, Stockholm University, Stockholm, Sweden

ROBERT HALLBERG

National Oceanic and Atmospheric Administration/Geophysical Fluid Dynamics Laboratory, Princeton, New Jersey

(Manuscript received 6 July 2018, in final form 16 November 2018)

ABSTRACT

The role of oceanic background diapycnal diffusion for the equilibrium climate state is investigated in the global coupled climate model CM2G. Special emphasis is put on the oceanic meridional overturning and heat transport. Six runs with the model, differing only by their value of the background diffusivity, are run to steady state and the statistically steady integrations are compared. The diffusivity changes have large-scale impacts on many aspects of the climate system. Two examples are the volume-mean potential temperature, which increases by 3.6°C between the least and most diffusive runs, and the Antarctic sea ice extent, which decreases rapidly as the diffusivity increases. The overturning scaling with diffusivity is found to agree rather well with classical theoretical results for the upper but not for the lower cell. An alternative empirical scaling with the mixing energy is found to give good results for both cells. The oceanic meridional heat transport increases strongly with the diffusivity, an increase that can only partly be explained by increases in the meridional overturning. The increasing poleward oceanic heat transport is accompanied by a decrease in its atmospheric counterpart, which keeps the increase in the planetary energy transport small compared to that in the ocean.

1. Introduction

The influence of the small scales of motion on the large ones is a classical problem in geophysical fluid dynamics. In this paper, we study a particular problem belonging to that class, namely, the effect of the background diapycnal turbulent diffusivity (referred to simply as background diffusivity) on the ocean circulation and its meridional heat transport. The background diffusivity is defined as the part of the diffusivity used in a climate model that is taken to be independent of the evolution of all other fields in the model. The background diffusivity can thus be a function of space but not of time and typical choices of background diffusivities are a constant, a fixed vertical profile or a profile that depends on latitude. How these different choices can influence the ocean general circulation is reviewed by Jayne (2009) and Jochum (2009). Current-generation climate models are considered simplistic if they have a turbulent diffusivity equal to the background diffusivity, and more comprehensive models have diffusivities that depend on a mixture of processes in addition to the background value. The background diffusivity used in comprehensive climate models has consequently evolved from being a parameterization of all oceanic mixing processes into a parameterization primarily of mixing occurring in the thermocline, separated from the primarily wind-driven mixing above and primarily tidally driven mixing below (Jayne and Laurent 2001; Simmons et al. 2004; Wunsch and Ferrari 2004).

Breaking of internal waves is thought to be the primary process driving mixing in the global ocean, although other processes are certainly also of importance (Wunsch and Ferrari 2004; Alford et al. 2016; Hieronymus and Carpenter 2016). The background diffusion can

Corresponding author: Magnus Hieronymus, hieronymus.magnus@gmail.com

DOI: 10.1175/JCLI-D-18-0438.1

© 2019 American Meteorological Society. For information regarding reuse of this content and general copyright information, consult the AMS Copyright Policy (www.ametsoc.org/PUBSReuseLicenses).

Brought to you by NOAA Central Library | Unauthenticated | Downloaded 08/28/24 07:12 PM UTC

therefore be thought of as a crude parameterization of an otherwise unparameterized part of the internal wave continuum. Here, we will discuss a set of sensitivity experiments where a comprehensive coupled climate model is exposed to an addition of spatially constant background diffusivity in several steps. Our aim with these experiments is not to run a set of physically motivated mixing scenarios; rather, it is to investigate the sensitivity of some key climate parameters to the highly variable and largely unknown strength of ocean mixing.

The oceanic meridional overturning circulation (MOC) is probably the part of the general circulation whose dependence on the diffusivity has the richest history, going back at least to Robinson and Stommel (1959) and Munk (1966). Much work has been done on scaling relations in theoretical or simplified models (see, e.g., Bryan and Cox 1967; Bryan 1987; Samelson and Vallis 1997; Ito and Marshall 2008; Den Toom and Dijkstra 2011), while little work on the subject has been done in comprehensive climate models owing to the great computational cost of running such models. Here, however, we investigate the role of the background diffusivity in a comprehensive state-of-the-art coupled atmosphere–ocean general circulation model (AOGCM).

The most classical scaling for the Atlantic meridional overturning circulation (AMOC) with diffusivity suggests that $\Psi \propto \kappa^{2/3}$ (Robinson and Stommel 1959; Bryan and Cox 1967; Nikurashin and Vallis 2012), where Ψ is the overturning strength and κ the diffusivity. Scaling theory for the Southern Ocean overturning suggests $\Psi \propto \kappa^{1/2}$ (Ito and Marshall 2008; Nikurashin and Vallis 2011). These scalings pertain to diffusively driven overturnings; however, our current understanding of the AMOC suggests that it is only partly driven by mixing. The other forcing agent is adiabatic, wind-driven upwelling along density surfaces in the Southern Ocean (Toggweiler and Samuels 1998). This adiabatic pathway can sustain an overturning even in the absence of interior-ocean mixing, so the role of diffusion might not be as prominent as the $\Psi \propto \kappa^{2/3}$ scaling suggests (Nikurashin and Vallis 2012). Scaling theories have, generally speaking, been quite successful in describing the MOC behavior in simplistic models, while they have had less success in capturing the behavior of coupled models and models with highly localized mixing (Simmons et al. 2004; Dalan et al. 2005; Saenko 2006; Jayne 2009). However, localized stratification-dependent mixing has been treated successfully in scaling theories (Nilsson et al. 2003).

The dependence of the oceanic meridional heat transport on diffusivity has attracted somewhat less attention than that of the meridional overturning circulation, although several notable studies exist (Dalan et al. 2005; Saenko 2006; Vallis and Farneti 2009; Msadek et al. 2013). The planetary meridional energy transport consists of both oceanic and atmospheric contributions and is of great scientific as well as societal interest because of its influence on regional climate. Stone (1978) found the magnitude of the planetary energy transport to depend primarily on the solar constant, the size of Earth, the tilt of Earth's axis, and the hemispheric mean albedo. It is therefore thought to be relatively weakly dependent on the dynamics of the atmosphere–ocean system, while its individual components are not. Held (2001) demonstrated that the meridional heat transport in the ocean exceeds that in the atmosphere close to the equator, while the atmospheric transport exceeds the oceanic one at midlatitudes. Furthermore, Vallis and Farneti (2009) demonstrated that the oceanic heat transport at midlatitudes could exceed that in the atmosphere if the ocean basins were wider or the rotation rate of the planet were different. The oceanic heat transport, which is the primary focus of this article, is thus more or less on par with the atmospheric on large areas of the globe and is therefore a key component of the climate system.

The oceanic meridional overturning and meridional heat transport are strongly connected (Boccaletti et al. 2005; Msadek et al. 2013), and both of them tend to increase with increased diffusivity in experiments with uniform diffusivities (Bryan 1987; Vallis and Farneti 2009). Experiments with more realistic localized mixing have shown that the spatial pattern of the diffusivity perturbation can be more important for the heat transport than the average perturbation (Saenko 2006; Jayne 2009). For example, Jayne (2009) found, using an ocean-only GCM, that increasing the diffusivity in the upper ocean increased the meridional oceanic heat transport, while diffusivity changes in the deep ocean gave no noticeable change in the heat transport. Here, we will utilize a technique spearheaded by Ferrari and Ferreira (2011) and Zika et al. (2013) to look at the heat transport due to individual cells in the meridional overturning streamfunction. We will also split the overturning and heat transport into separate basins to present a more detailed view of the ocean heat transport and its dependence on diffusivity.

A central oceanographic question is how the MOC and ocean stratification depend on their forcing. Conceptual models have been developed that describe the oceanic state given prescribed surface buoyancy fluxes, diapycnal mixing and large scale wind forcing. However, in the real coupled ocean–atmosphere system these forcing agents of the ocean circulations are not prescribed but emergent properties of the coupled system. Here, we examine the coupled ramifications of changes in

Brought to you by NOAA Central Library | Unauthenticated | Downloaded 08/28/24 07:12 PM UTC

TABLE 1. Additional spatially homogeneous background diffusivity and the globally averaged model diffusivity between 500 and 1000 m in our integrations. Units are $m^2 s^{-1}$.

	d0	d1	d2	d4	d6	d8
Additional background κ	0	1×10^{-5}	2×10^{-5}	4×10^{-5}	6×10^{-5}	8×10^{-5}
500–1000-m average κ	0.9×10^{-4}	1.0×10^{-4}	1.1×10^{-4}	1.3×10^{-4}	1.5×10^{-4}	1.7×10^{-4}

interior ocean diapycnal mixing, which affects cloud cover, surface winds, sea ice distribution, and ocean circulation through a rage of coupled feedbacks in our set of climate model simulations.

2. Model description

We use the global coupled climate model CM2G. CM2G is the physical part of the Geophysical Fluid Dynamics Laboratory Earth System Model with GOLD component (GDFL-ESM2G, herein ESM2G; Dunne et al. 2012) that participated in phase 5 of the Coupled Model Intercomparison Project (CMIP5). It contains the atmospheric model, version 2 (AM2; Anderson et al. 2004), the land model, version 3.0 (LM3.0; Milly et al. 2014), the sea ice model (SIS; Winton 2000), and the isopycnal ocean model GOLD (Hallberg and Adcroft 2009). The atmosphere, land, and sea ice radiative components are coupled every 30 min, while the ocean–atmosphere tracer coupling time step is 2 h. The resolution in the atmosphere is 2° latitude by 2.5° longitude with 24 vertical levels. The oceanic resolution is a nominal 1° with equatorial refinement in the horizontal and 63 vertical levels. The lower 59 vertical levels are isopycnal, while the upper 4 vertical levels are mixed and buffer layers. A pressure-dependent nonlinear equation of state (EOS) is used everywhere except in the definition of the isopycnal levels, which are defined in terms of potential density referenced to 2000-m depth and are computed using the same EOS. Turbulent diapycnal ocean mixing in the isopycnal interior is parameterized using several different components: tidal mixing (St. Laurent et al. 2002), a stratification-dependent diffusivity based on Gargett and Holloway (1984), shear-driven mixing (Jackson et al. 2008), and a bottom boundary layer (Legg et al. 2006). Finally, there is a latitude-dependent background diffusivity with a minimum value of $2 \times 10^{-6} m^2 s^{-1}$ at the equator, which increases to $2 \times 10^{-5} m^2 s^{-1}$ at 30°N and 30°S (Harrison and Hallberg 2008). Isopycnal mixing is parameterized with a Laplacian operator, and isopycnal height diffusion is parameterized analogously to Gent and McWilliams (1990) with a slope-dependent mixing coefficient taking values between 10 and $900 m^2 s^{-1}$. Both the isopycnal and the diapycnal mixing coefficients are equal for temperature and salt.

In total we have done six steady-state CM2G integrations using preindustrial radiative forcing (intended to mimic 1860 conditions) that differ only by the addition of extra spatially homogeneous background diffusivity in five of them. Table 1 gives the values of additional background diffusivity in the runs and the naming convention. The value of the background diffusivity in the different runs varies by about an order of magnitude, where the smallest values give diffusivities in the thermocline that are comparable to observations, while the largest background diffusivity gives a thermocline diffusivity close to the canonical mean diffusivity of $10^{-4} m^2 s^{-1}$ inferred by Munk (1966) and Munk and Wunsch (1998). All six runs are started from a 3000-yr-long integration with the same preindustrial forcing and are then integrated for an additional 2200 years each. Our analyses are done on an average of the last 100 years. The trend in volume-mean ocean temperature at the end of the integration is less than 0.02°C $century^{-1}$ in all runs. The largest trend occurs in d4 where it reaches 0.018°C $century^{-1}$ and the average trend between the runs is 0.0068°C $century^{-1}$. The average trend in our simulations is smaller than that found in the long preindustrial control runs of ESM2M (0.038°C $century^{-1}$) and ESM2G (0.01°C $century^{-1}$) used for CMIP5 (Dunne et al. 2012). For volume-averaged salinity, the trend is largest in d0 where it reaches 0.45×10^{-5} PSU $century^{-1}$, while the average salinity trend over the runs is 0.16×10^{-5} PSU $century^{-1}$.

Dunne et al. (2012) did a detailed comparison of the preindustrial control simulations of ESM2G and ESM2M to present-day observations, and their results for ESM2G are essentially identical to those from our d0 run. A comparison of present-day observation to modeled 1860 conditions is of course hampered by the fact that Earth has warmed since 1860 and a general cold bias was also found in both models. Nonetheless, Dunne et al. (2012) found many climate metrics to be in good agreement with observations in both models, with ESM2G being slightly closer to the observations in the ocean interior and ESM2M at the surface. The overturning transport and heat transport agree rather well with observations. The maximum Atlantic overturning at 26.5°N in d0 is 21.4 Sv ($1 Sv \equiv 10^6 m^3 s^{-1}$) compared to 18.5 Sv estimated from the RAPID–MOCHA array between April 2004 and October 2007 (Msadek et al. 2013). The Atlantic meridional heat

Brought to you by NOAA Central Library | Unauthenticated | Downloaded 08/28/24 07:12 PM UTC

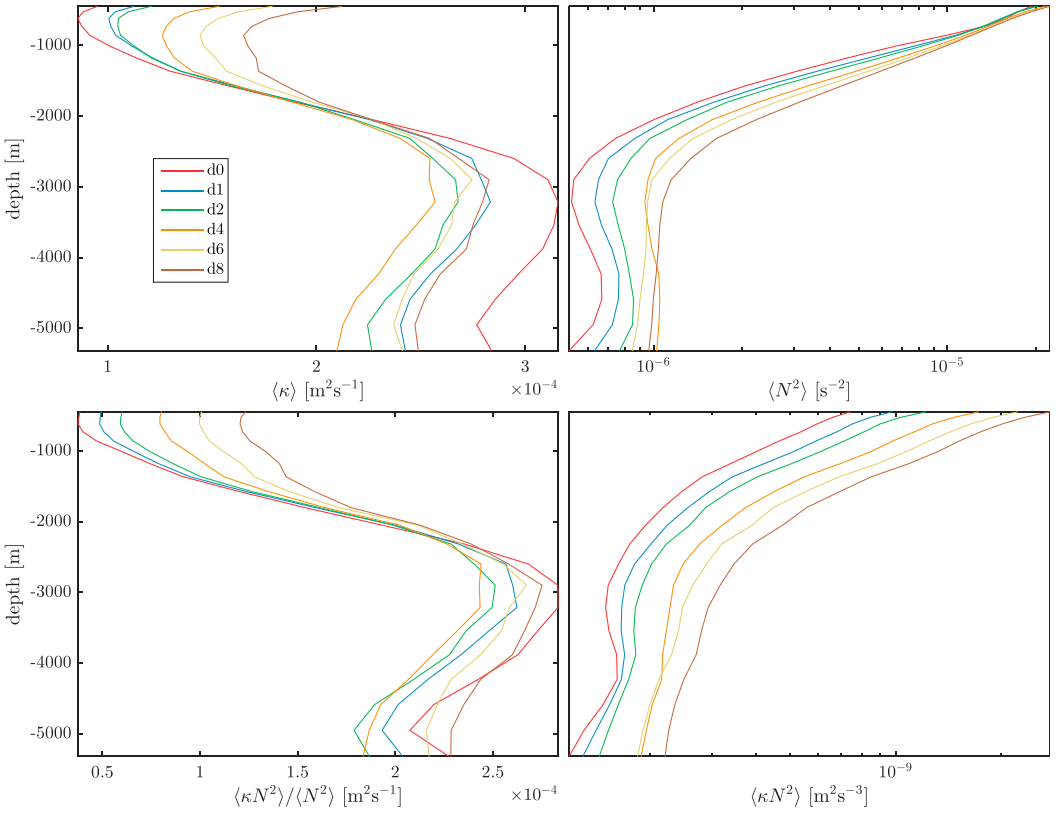

FIG. 1. Horizontally averaged κ, N^2, and κN^2 and a stratification average of κ from our six runs. The x axes for N^2 and κN^2 are logarithmic; κN^2 is calculated from long time averages of κ, and N^2 is calculated online by the model, so it shows $\overline{\kappa}\,\overline{N^2}$ rather than $\overline{\kappa N^2}$.

transport derived from the RAPID array is 1.33 PW (Johns et al. 2011), while that in d0 is 1.14 PW.

3. General flow description

This section shows how the general flow characteristics change in our AOGCM as a function of the background diffusivity. The background diffusivity is, as was discussed in the preceding section, only one of several schemes that contributes to the diffusivity in the model. The actual diffusivity in the model is therefore set by a complex interplay of processes, and a run with smaller background diffusion may actually be more diffusive in some regions than one with a larger value. Figure 1 shows horizontally averaged κ and N^2 between 500 m and the ocean floor in the top two panels and a stratification-weighted average of κ in the lower-left panel. The stratification-weighted average is defined as $\langle \kappa N^2 \rangle / \langle N^2 \rangle$, where the angle brackets indicate a horizontal average at a fixed depth level. The horizontal average of κ is quite strongly affected by large values found in weakly stratified areas, while the stratification-weighted average gives less weight to such areas. This is noticeable in the upper 1000 m where the stratification-weighted average is much closer to observed values in the thermocline, which are typically on the order of $10^{-5}\,\mathrm{m^2\,s^{-1}}$ (Ledwell et al. 1993).

The model's diffusivity is seen to have a complex response to changes in the background diffusivity; above a depth of around 2000 m, the diffusivities are ordered according to the size of the background diffusivity, while the ordering in the deep ocean is not a monotonic function of the background diffusivity either for the stratification-weighted or for the directly horizontally average diffusivity. The reason for the complex ordering in the deep ocean is that the diffusivity scheme that is most prevalent there, that of St. Laurent et al. (2002), gives diffusivities that are inversely proportional to the stratification ($\kappa_{\mathrm{StL}} \propto N_b N^{-2} \approx N^{-1}$, where N_b is the value of N at the ocean floor). The change in the deep ocean diffusivity with background diffusivity is therefore given by the sum of a positive contribution from addition of background diffusivity and a, mostly, negative contribution from changes in the stratification. The ordering of the profiles in the upper ocean meanwhile strongly suggests a controlling influence of the background diffusivity.

Brought to you by NOAA Central Library | Unauthenticated | Downloaded 08/28/24 07:12 PM UTC

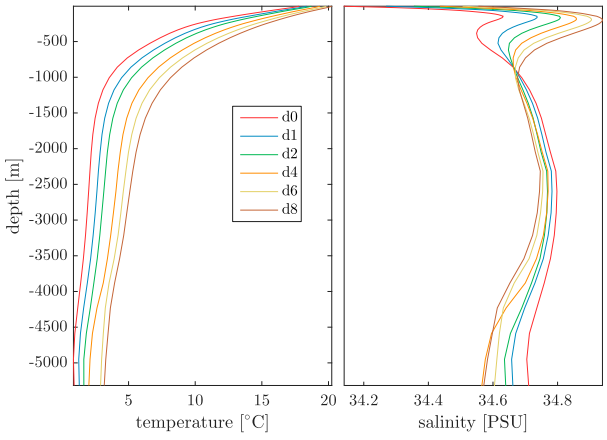

FIG. 2. Horizontally averaged (left) temperature and (right) salinity profiles from our different runs.

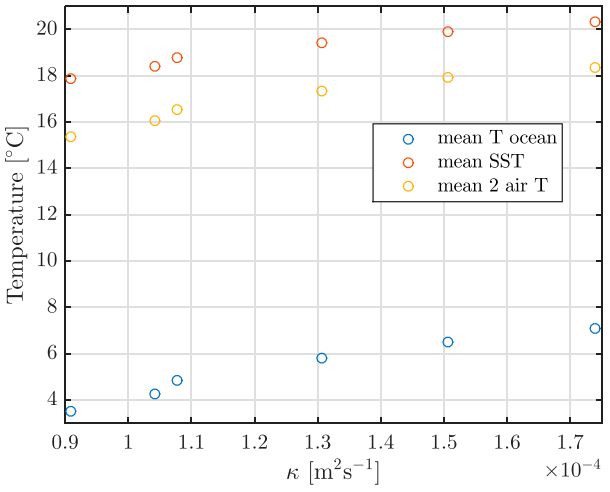

FIG. 3. Volume-mean ocean temperature, SST, and 2-m air temperature over the ocean as a function of the mean κ between 500- and 1000-m depth.

The conventional wisdom, which applies primarily when the diffusivity can be assumed to be constant, is that a larger diffusivity gives a thicker thermocline and a more stratified deep ocean (Munk 1966; Munk and Wunsch 1998; Nikurashin and Vallis 2011). Our simulations support this picture, but also show that the increased stratification in the deep ocean is caused by the increased diffusivity in the thermocline, while it is not necessary for the diffusivity in the deep ocean to increase to achieve such a change. A reason for this is the dependence of κ on N in the deep ocean. When $\kappa \propto N^{-1}$, as it is in the deep ocean in our simulations owing to the St. Laurent et al. (2002) parameterization, we get a diapycnal diffusive buoyancy flux κN^2 that is proportional to N. That is, an increase in the buoyancy flux implies a stronger stratification. Figure 1 shows that the downward buoyancy flux increases with increasing background diffusivity. Our change of the background diffusivity affects the diffusivity directly primarily in the thermocline and increases the downward buoyancy flux there. The response of the deep ocean is also to increase the buoyancy flux, and when $\kappa \propto N^{-1}$ this implies a stronger stratification.

Figure 2 shows the horizontally averaged salinity S and potential temperature T (referred to simply as temperature) profiles in the different runs. The temperature profile shows a rather uniform increase with increased background diffusivity, while the salinity stratification changes so that the deep-ocean salinity decreases and the upper-ocean salinity increases with increased background diffusivity. A likely reason for the changes in the deeper part of the salinity profile is that there is much less sea ice in the Southern Ocean in the runs with more background diffusivity, which gives less brine release and thus fresher deep waters. The erosion of the salinity minimum between 500 and 1000 m in the more diffusive runs is a sign of vanishing Antarctic Intermediate Waters (AAIWs). The salinity changes are such that they make the ocean below 1000 m less stably stratified with increased background diffusivity. That is, they do the opposite to the temperature changes. However, the increase in mean temperature works in concert with the nonlinearities of the equation of state to make the salinity contribution smaller. The thermal expansion coefficient increases with increased temperature, while the haline contraction coefficient is nearly constant. The warming thus works to downplay the effects of the changes to the haline stratification, and the overall stratification becomes more dominated by the thermal contribution.

The volume-mean ocean temperature, mean SST, and mean 2-m air temperature over the ocean as a function of diffusivity are shown in Fig. 3. As a measure of the diffusivity in the model, we have chosen to use the average κ between 500 and 1000 m (values are given in Table 1) here and throughout the paper. This somewhat arbitrary choice is motivated by the fact that the diffusivities in this depth range in the model are ordered according to the magnitude of the added background diffusivity, and that many features of the model, such as, for example, the overturning strength and the mean temperature, are monotonic functions of the added background diffusivity. Our choice of κ thus ensures that the monotonicity is kept and that the values reflect the actual diffusivity in the model. Figure 4 shows κ as a function of the added background diffusivity.

The volume-mean temperature increases more than the SST, and the increase in temperature is largest in the thermocline. The equilibrium climate sensitivity of ESM2G (an Earth system model based on CM2G) to a doubling of

Brought to you by NOAA Central Library | Unauthenticated | Downloaded 08/28/24 07:12 PM UTC

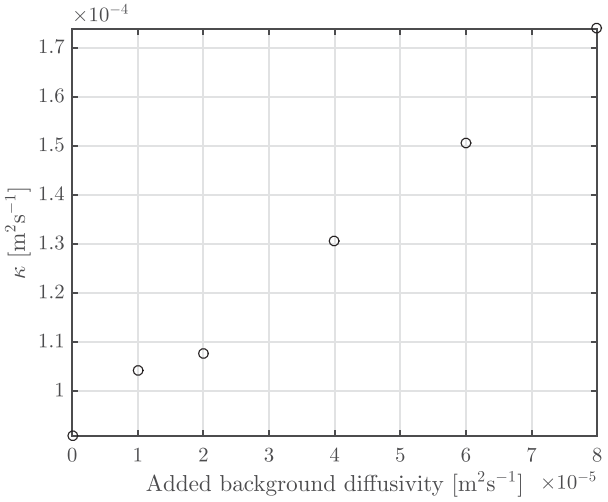

FIG. 4. The mean κ between 500- and 1000-m depth as a function of the added background diffusivity.

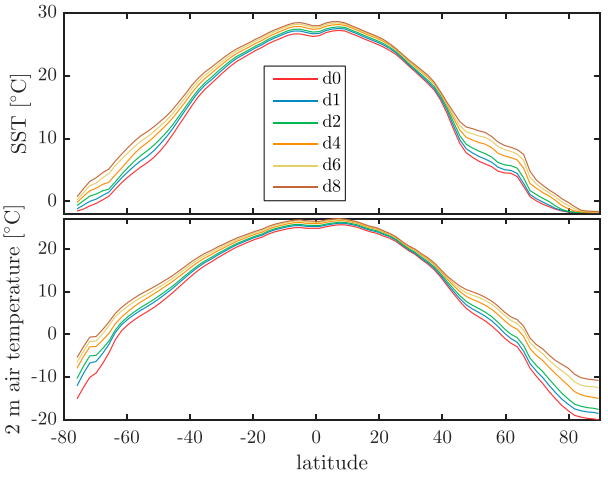

FIG. 6. Zonal-mean (top) SST and (bottom) 2-m air temperature over the ocean.

CO_2 has been estimated at 3.2°C (Winton et al. 2013), so the mean 2-m air temperature change in the most diffusive run is similar in magnitude to that caused by a doubling of CO_2. Neither the SST nor the volume-mean temperature is a linear function of κ. The mean surface temperature change is, however, linearly related to the change in the outgoing longwave (or equivalently net shortwave) radiation at the top of the atmosphere (TOA) as can be seen in Fig. 5. The equivalence in magnitude of the long- and shortwave radiation changes at the TOA is required for a steady state.

The zonal-mean SST and 2-m air temperature over the ocean are shown in Fig. 6. The temperature maximum tends to coincide with the time-mean position of the intertropical convergence zone (ITCZ), and the two peaks on either side of the equator show that our model suffers from the common double-ITCZ bias (Oueslati and Bellon 2015). The differences between the runs are largest at high latitudes, and there is no strong asymmetry with large Arctic and weak Antarctic warming as is common in transient simulations of CO_2-induced warming (Marshall et al. 2014). There is also a general pattern where the SSTs, especially equatorward of latitude 40°N, increase more in the Southern Hemisphere than in the Northern Hemisphere. The largest temperature differences in the Northern Hemisphere occur approximately between latitudes 40° and 60°N and coincide with the maximum

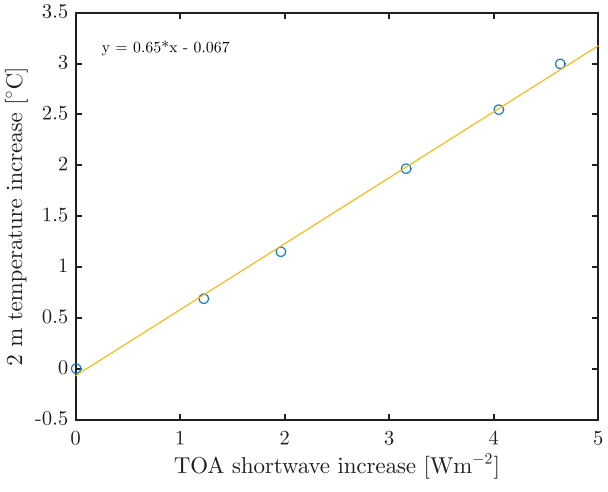

FIG. 5. Increase of global-mean 2-m air temperature as a function of the increase of the area-averaged net shortwave radiation at the TOA. The shortwave flux is defined positive when downward.

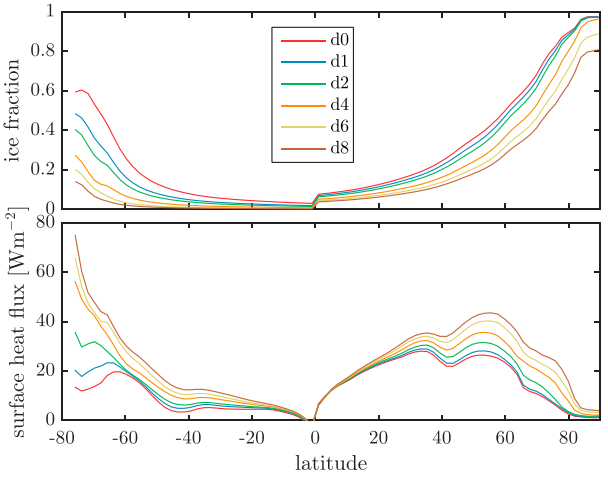

FIG. 7. (top) Mean ice fraction and (bottom) mean upward surface heat flux. Both panels show quantities that are area averaged poleward of the latitude given on the x axis. The values shown at latitude 80°N are thus the area-averaged values between 80° and 90°N. The equatorial discontinuity occurs because the computation changes direction there.

Brought to you by NOAA Central Library | Unauthenticated | Downloaded 08/28/24 07:12 PM UTC

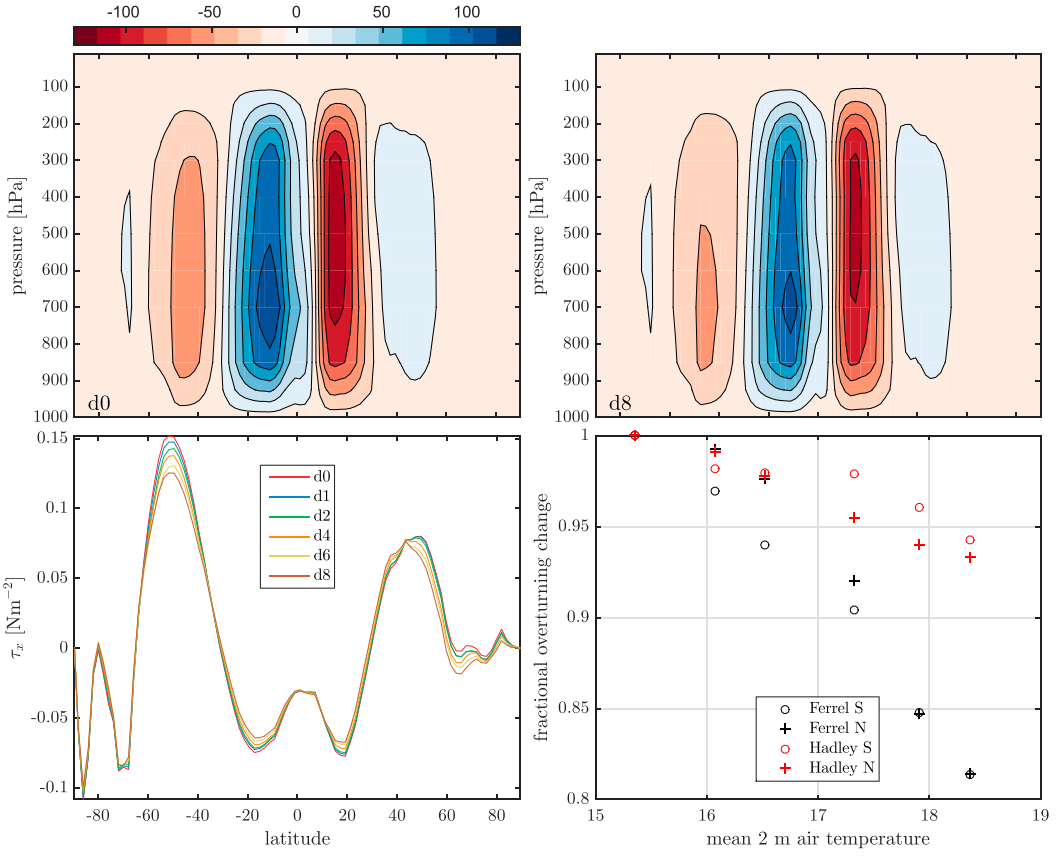

FIG. 8. (top left) Atmospheric meridional overturning streamfunction in d0, (top right) atmospheric meridional overturning streamfunction in d8, (bottom left) zonal-mean zonal wind stress, and (bottom right) fractional change in the overturning strength as a function of global-mean 2-m air temperature. In the bottom right panel, "Ferrel S" is the southern Ferrel cell, "Ferrel N" is the northern Ferrel cell, and the same conventions is used for the Hadley cells. The overturning strength is in units of Sv ($1\,\text{Sv} = 10^9\,\text{kg}\,\text{s}^{-1}$), and contours are drawn every 20 Sv.

in the MOC and large changes in the oceanic meridional heat transport discussed in section 5.

The sea ice cover, which directly affects the albedo and indirectly the radiative balance through its effect on moisture, exhibits a strong control on climate (Ferrari et al. 2014; England et al. 2017). Figure 7 shows the mean ice fraction and mean upward surface heat flux, both averaged poleward of the latitude given on the x axis. There is a strong decline in sea ice, especially in the Southern Hemisphere, and this decline is coincident with large increases in the surface heat flux. The upward surface heat flux integrated poleward of a given latitude, equals, in a steady state, the poleward oceanic meridional heat flux, which increases with diffusivity. Given that our diffusivity changes affect the ocean most strongly in the thermocline, it seems more reasonable for the sea ice reduction and increased surface fluxes to be a consequence of the increased oceanic meridional heat flux rather than the other way around. The oceanic meridional heat flux is also closely tied to the MOC, which scaling theory suggests increases with increased diffusivity. Moreover, the largest sea ice reduction occurs in the Southern Hemisphere where the MOC maximum occurs under significant sea ice cover. In the Northern Hemisphere, the sea ice reduction is more modest and the MOC maximum there occurs southward of the areas of significant sea ice cover. The ice albedo effect alone, however, is certainly not strong enough to give the warming observed in the model and it is quite remarkable that a diapycnal diffusivity change of about a factor of 2 is enough to induce a climate feedback loop that results in a mean surface temperature increase of about 3°C.

The polar amplification of the warming decreases the meridional temperature gradient, which in turn leads to weaker zonal winds. This effect is prominent in the high-latitude Southern Hemisphere but not in the Northern Hemisphere, as can be seen in Fig. 8. The figure also shows the atmospheric meridional overturning circulation from experiments d0 and d8 and the fractional change in the strength of the Hadley and

Brought to you by NOAA Central Library | Unauthenticated | Downloaded 08/28/24 07:12 PM UTC

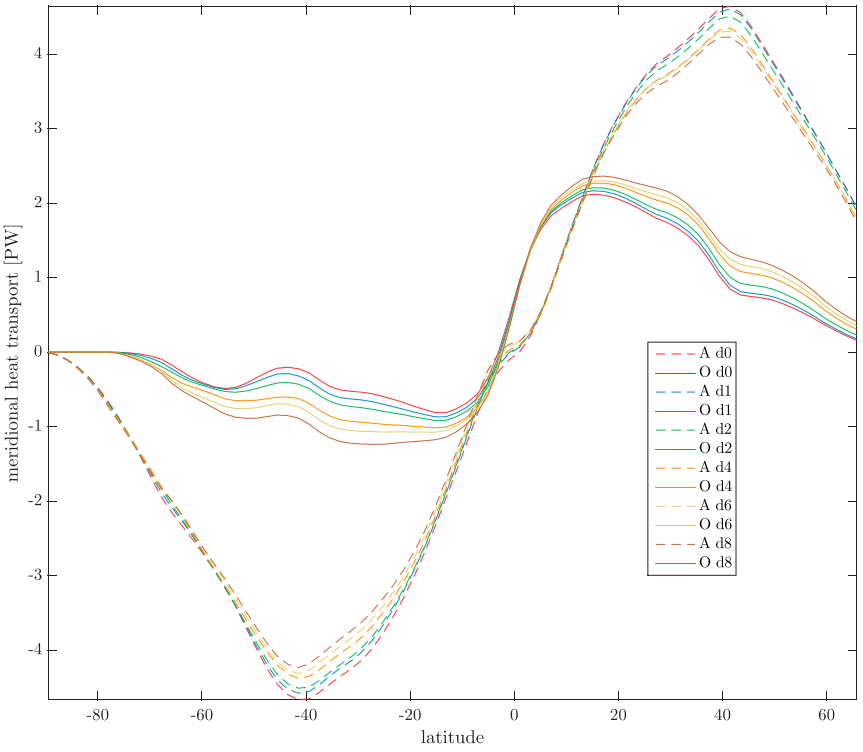

FIG. 9. Oceanic and atmospheric meridional heat transport. *A* denotes atmosphere and *O* denotes ocean. The heat transports are calculated on the ocean model's native tripolar grid, and the latitudes north of 65°N are therefore not accurate and have been excluded.

Ferrel cells as a function of global-mean temperature in the different experiments. The weakening of the Southern Hemisphere westerly winds is coincident with a drop in the strength of the Ferrel cell. Such a pattern was also found by Rojas (2013) while comparing Last Glacial Maximum, present-day, and high-CO_2 simulations. The fractional changes in the overturning strength are very similar in the two hemispheres for both cells. A weakening of the Hadley cells in response to CO_2-induced global warming in the range 0%–4% K^{-1}, with a mean of 1.2% K^{-1}, was found in an ensemble of climate models by Lu et al. (2007). Our Hadley cells weaken by about 2% K^{-1}, and the response is thus within the range of that seen for CO_2-induced warming.

Figure 9 shows the atmospheric and oceanic energy transports in the different runs. A note on how those are calculated is found in the appendix. The figure shows that the increased poleward heat transport in the ocean is nearly compensated by a decrease in the atmospheric energy transport. This compensation agrees well with the findings of Stone (1978) that the planetary meridional energy transport is insensitive to changes in the general circulation of the atmosphere and ocean, as was discussed in the introduction. There is, however, a small net increase in the meridional energy transport, which shows that the warming-induced increase in the outgoing longwave at high latitudes is nearly, but not fully, compensated for by increased incoming shortwave radiation due to albedo reductions. The near compensation between the atmospheric and oceanic energy transports and the rather large surface temperature increase also suggests that the mean surface temperature is more sensitive to oceanic energy transport than to atmospheric. A plausible reason for the difference in sensitivity is that an increased poleward oceanic heat transport implies, in a steady state, an equal increase in the upward surface heat flux because of the insulating boundary conditions used at the ocean floor. An increase in the poleward atmospheric energy transport, however, does not necessarily imply any change in the surface flux because of the open boundary condition at the TOA. Changes in the poleward oceanic heat transport thus imply changes in the surface energy fluxes, while changes in the meridional atmospheric energy transport can occur, at least in principle, without any changes occurring at the surface.

4. Meridional overturning

Here, we consider the dependence of the strength of the meridional overturning circulation on the diffusivity.

Brought to you by NOAA Central Library | Unauthenticated | Downloaded 08/28/24 07:12 PM UTC

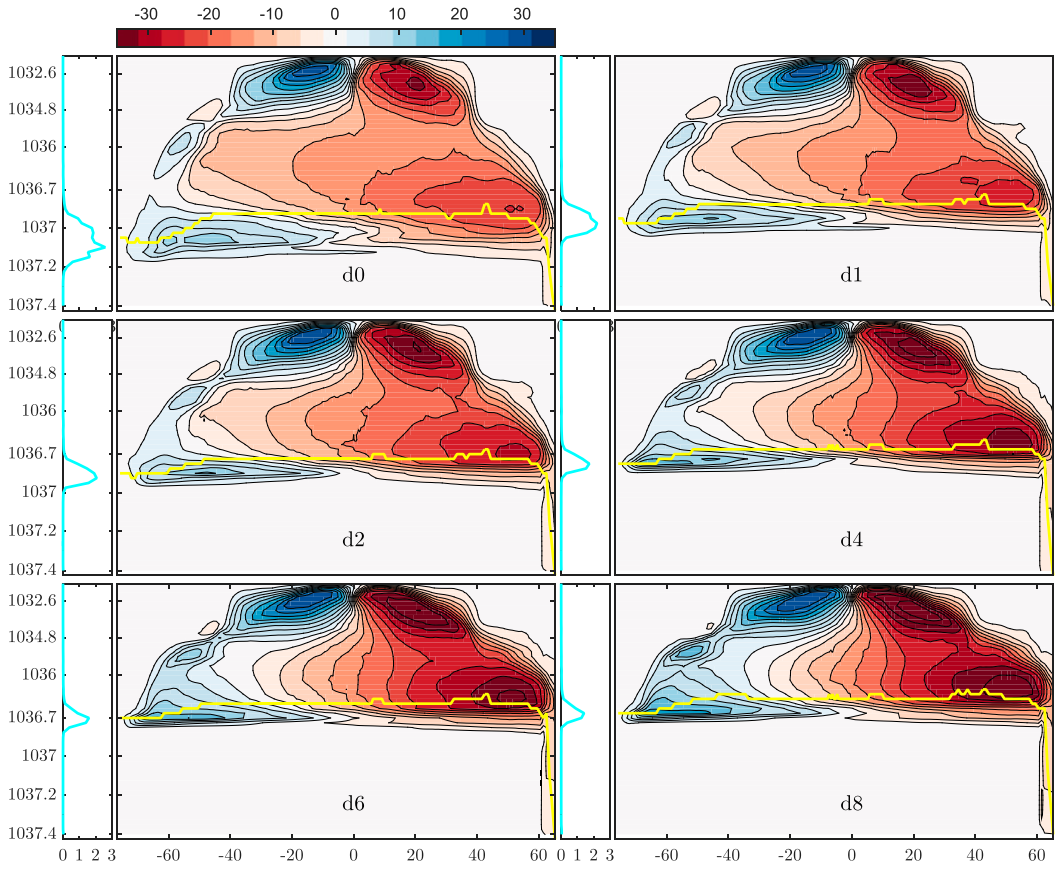

FIG. 10. Meridional residual overturning streamfunctions (Sv) in density–latitude coordinates. Contours are drawn every 3.5 Sv. The cyan lines in the side panels show the incrop area (de Lavergne et al. 2016) in units of $10^{15}\,\mathrm{m}^2\,(\mathrm{kg\,m}^{-3})^{-1}$. The yellow line is the zonally averaged 2000-m-depth contour. The transports are calculated on the ocean models native tripolar grid and the latitudes north of 65°N are therefore not accurate and have been excluded. The density variable used is potential density referenced to 2000 m.

Figure 10 shows the residual[1] overturning streamfunctions. The subtropical cells (STCs) in the low-latitude upper ocean appear to be rather insensitive to the variations in background diffusivity. However, it is clear from the figure that both the interhemispheric overturning cells, the upper cell associated with North Atlantic Deep Water (NADW) and the lower cell associated with Antarctic Bottom Water (AABW), increase in strength with increased background diffusivity. The cyan lines in the side panels show the incrop area, that is, the area of the sea floor occupied by a particular density class (de Lavergne et al. 2016). The maximal overturning in the lower cell clearly coincidences with the peak incrop area in all our simulations, lending further credence to the hypotheses that the abyssal overturning is strongly constrained by the bottom intensification of mixing and the no normal flux condition at the ocean floor (Ferrari et al. 2014, 2016; de Lavergne et al. 2016). The yellow lines show the 2000-m depth contour that approximately separates the region above where the horizontally averaged diffusivity increases as a function of background diffusivity from that below where the response to increased background diffusivity is nonmonotonic (see Fig. 1). The diffusivity is thus increasing with increased background diffusivity over most of the upper cell, while it changes erratically over the lower cell. The nonmonotonic diffusivity changes coincide with a monotonic increase in the strength of the lower cell, which precludes a scaling relationship. The MOC strength has been shown to be sensitive not only to the vertical profile of $\langle\kappa\rangle$ but also to its horizontal distribution (Simmons et al. 2004; Saenko 2006; Jayne 2009). Saenko (2006) suggested therefore that $\langle\kappa N^2\rangle$ was a more appropriate scaling quantity than $\langle\kappa\rangle$. We will return to this idea later in the section.

[1] These streamfunction contain both the resolved advection and the parameterized thickness diffusion that is commonly parameterized as Gent and McWilliams (1990) in z-coordinate models.

Brought to you by NOAA Central Library | Unauthenticated | Downloaded 08/28/24 07:12 PM UTC

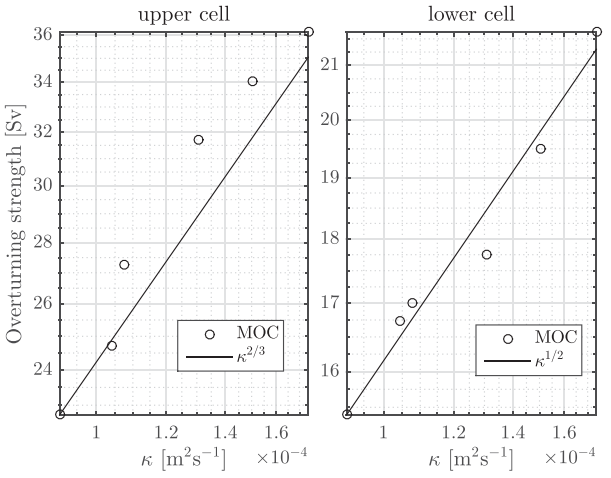

FIG. 11. Scaling of the overturning cells with diapycnal diffusivity, plotted as the maximum overturning against the horizontally averaged κ between 500- and 1000-m depth.

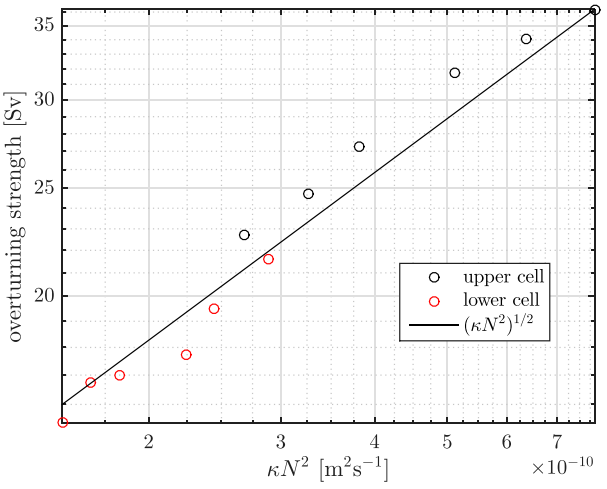

FIG. 12. Scaling of the overturning with κN^2, a proxy for the mixing energy; κN^2 is calculated as a horizontal average between 1000 and 2000 (3000 and 4000) m for the upper (lower) cell.

Apart from diffusivity changes, scaling theory also suggests that the MOC cells are sensitive to changes in meridional density differences and Southern Ocean wind stress. Several studies find that the strength of the upper cell depends on the meridional density difference as $\Psi \propto \Delta\rho^{1/3}$ (Robinson and Stommel 1959; Bryan and Cox 1967; Nikurashin and Vallis 2012), while Nikurashin and Vallis (2011, 2012) find that the upper cell scales with the Southern Ocean wind stress τ as $\Psi \propto \tau$ and the lower cell as $\Psi \propto \tau^{-1}$, both in the limit of weak diffusion. In our coupled simulations, both $\Delta\rho$ and τ evolve freely. The Southern Ocean wind stress decreases by about 20% from d0 to d8. This change is of the wrong sign to explain the evolution of the upper cell and too small to explain the increase in the lower cell. To look at the possible influence of changes in $\Delta\rho$ on the overturning, we have calculated the zonally averaged meridional density difference integrated cumulatively from the surface down to all fixed depth levels used for model output. Calculating from that $[\Delta\rho(d8)/\Delta\rho(d0)]^{1/3}$ at all depth levels gives at most a value of 1.1, so differences in the overturning strengths due to changes in the meridional density gradient should not exceed 10%.

Figure 11 shows the scaling of the upper and lower cell with the horizontally averaged diffusivity between 500- and 1000-m depth. The upper cell follows approximately the $\Psi \propto \kappa^{2/3}$ scaling. This is perhaps not so surprising since the overturning maximum occurs at about 1000 m, so the diffusivity there will be close to the scaling diffusivity and dominated by the background diffusivity. The diffusivity is also rather large, so the adiabatic pathway, where deep water formed in the Northern Hemisphere upwells along density surfaces in the Southern Ocean (Toggweiler and Samuels 1998), should be less important than the diabatic one. The lower cell follows an approximate $\Psi \propto \kappa^{1/2}$ scaling with the horizontally averaged diffusivity between 500- and 1000-m depth. We believe this scaling to be incidental and depending on a connection between the κ used in the scaling and κN^2 farther down in the water column.

The volume integral of $\rho_0 \kappa N^2$ is the so-called mixing energy (Munk and Wunsch 1998; Nycander 2011), which in a steady state balances the conversion term between potential and kinetic energy in the potential energy equation. The mixing energy is also the scaling quantity favored by Saenko (2006) in his experiments with localized versus nonlocalized mixing. On the other hand, Hogg et al. (2013) found that globally averaged energy quantities were difficult to connect to the strength of the overturning. In an attempt to get around this difficulty, we calculated $\langle \kappa N^2 \rangle$ between the depths of 1000 and 2000 (3000 and 4000) m to compare with the strength of the upper (lower) cell. Figure 12 shows the resulting scaling, which to a fair approximation for both cells is $\Psi \propto (\kappa N^2)^{1/2}$ [the least squares estimates are $\Psi \propto (\kappa N^2)^{0.45}$ for the middle cell and $\Psi \propto (\kappa N^2)^{0.48}$ for the lower]. It is pleasing to see that the same scaling now prevails for both cells. However, Jayne (2009) found the mixing energy to scale with the strength of the upper but not with the lower cell, so more work is clearly needed to determine the robustness of this empirical result.

5. Meridional heat transport

In section 3, it was shown that increased background diffusion leads to an increased oceanic meridional heat

Brought to you by NOAA Central Library | Unauthenticated | Downloaded 08/28/24 07:12 PM UTC

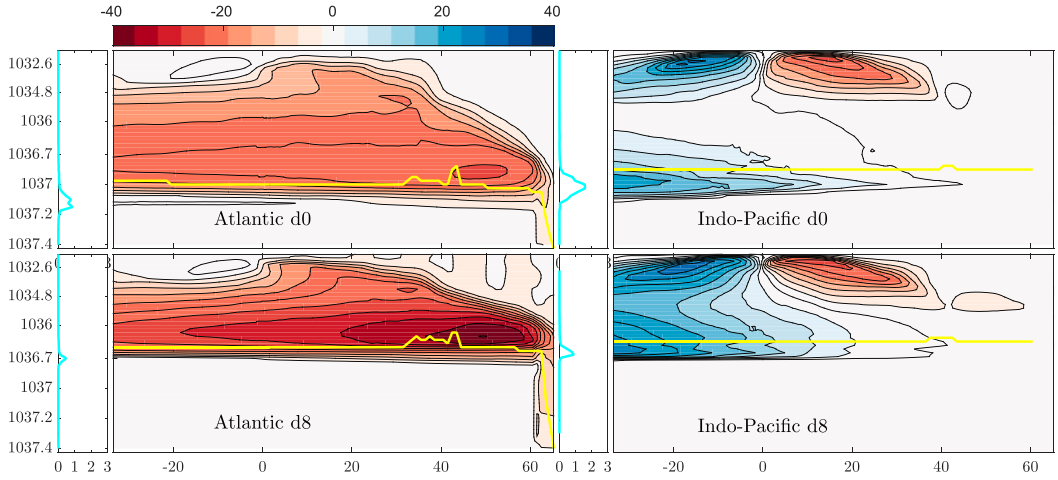

FIG. 13. As in Fig. 10, but with separate streamfunctions for the (left) Atlantic and (right) Indo-Pacific basin for the (top) d0 and (bottom) d8 simulations.

transport. In this section, we will examine how this increase is tied to changes in the ocean circulation. Our focus is on the advective meridional heat fluxes, which are much larger than their diffusive counterparts. As is discussed in the appendix, these fluxes depend on the choice of reference temperature when the net volume transport through a zonal transect is nonzero. This inconvenience means that the heat transports are not generally comparable between models unless the accompanying volume transports are zero. Ferrari and Ferreira (2011) therefore proposed a method where heat fluxes due to individual closed streamfunction cells can be compared, since such cells transport no net mass. We will adopt the same methodology here, but with one minor difference. Ferrari and Ferreira (2011) used a streamfunction in temperature–latitude coordinates in their analysis. This is a convenient choice when calculating heat transports since those are given by an integral over the streamfunction. We will, however, keep working in density–latitude coordinates to make this section more complementary to the preceding one. The heat flux due to a cell occupying the densities between ρ_1 and ρ_2 is then given by

$$H_T = \rho_0 c_p \int_x \int_{z(\rho_1)}^{z(\rho_2)} v T dx dz. \quad (1)$$

We have chosen to look at the meridional heat transport due to individual streamfunction cells at latitudes 20°N and 20°S, which is approximately where the oceanic meridional heat transport reaches its maximum. The diagnostics are carried out individually on the Atlantic and Indo-Pacific basins. The streamfunctions for the respective basins are shown in Fig. 13. In the Atlantic at 20°S, there are three closed streamfunction cells (i.e., cells that are separated by a zero streamline): a weak lower cell, a strong upper cell, and a weak STC. In the South Pacific, there is only one closed cell because the STC and the lower cell are connected and form a joint large cell. This is clearly seen in the panel showing the d8 experiment but is true also for the d0 experiment and the others.

Figure 14 shows the strengths of the different overturning cells and their associated heat transport. The heat transport of a streamfunction cell scales as

$$H_T \propto \Psi \Delta T, \quad (2)$$

where ΔT is the flow-weighted temperature difference between north- and southward flowing water in the cell (Saenko 2006; Vallis and Farneti 2009). The heat flux carried by a circulation cell is thus linearly proportional both to Ψ and ΔT. The heat transport in the Atlantic at 20°S is dominated by the large upper cell and is consequently equatorward. The heat transport of the upper cell increases with increased diffusivity in response to increases in Ψ. The ΔT changes over the cell [estimate using Eq. (2)] are not monotonic with the diffusivity, but give a mostly opposing effect, of secondary importance, as ΔT decreases from 7.7°C in d0 to 7.1°C in d8. The poleward heat transport in the South Pacific is larger than the equatorward flux in the South Atlantic. It also increases faster with increasing diffusivity, although the volume transport increases more slowly than that in the Atlantic upper cell. The reason is that ΔT in the South Pacific increases from about 11°C in d0 to 14°C in d8. It is plain to see from Fig. 13 that the ΔT increase results from a stronger connection between the upper and lower parts of the cell in the more

Brought to you by NOAA Central Library | Unauthenticated | Downloaded 08/28/24 07:12 PM UTC

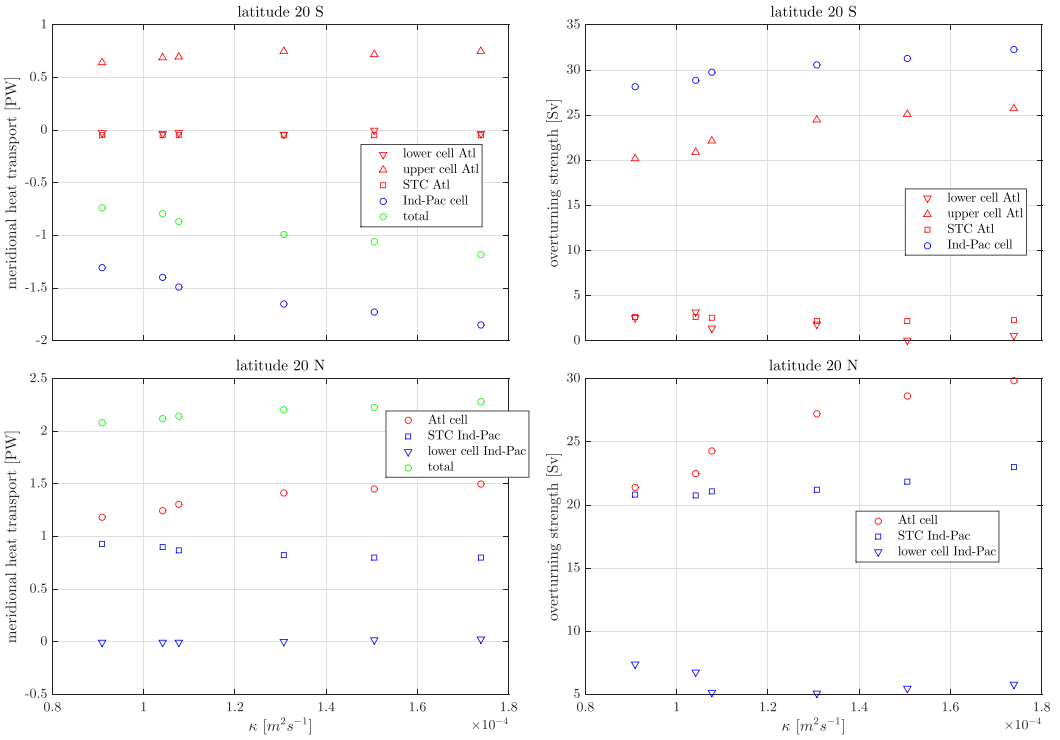

FIG. 14. Overturning cell strengths and heat transport as a function of κ at (top) 20°S and (bottom) 20°N. The heat flux calculations presented here are done offline, and the total heat flux calculation differs from the online version by less than 3%.

diffusive runs. That is, the increased diapycnal upwelling increases ΔT and consequently the meridional heat transport. This is the main reason why the total southward heat transport increases from 0.74 PW in d0 to 1.19 PW in d8.

At 20°N, there are three closed overturning cells: one in the Atlantic, which occupies the entire water column, and the STC and lower cell in the Indo-Pacific Ocean. The lower cell transports very little heat, so the poleward heat transport is achieved by the Atlantic cell and the Indo-Pacific STC. Both cells increase their circulation and decrease their ΔT with increasing diffusivity. The net effect is that the poleward heat transport increases in the Atlantic and decreases in the Indo-Pacific STC. This also means that the heat transport that is roughly equal in the Atlantic and the Indo-Pacific for small values of κ is nearly a factor of 2 larger in the Atlantic than in the Indo-Pacific for the largest κ. This is a huge difference given also that the Pacific basin is about twice as wide as the Atlantic.

It is clear from the above analysis that the overturning characteristics of a basin are key for determining its heat transport. The oceanic heat transport in both hemispheres is dominated by the basins where only one large overturning cell exists. Such cells exist in the North Atlantic and the South Pacific as a consequence of the Sverdrup transport, which is equatorward in the subtropical gyres, and the deep-water transport going in the same direction. These two large equatorward flows are primarily balanced by the poleward flow in the western boundary current (WBC) as is emphasized in Nof and de Bohr (2004). Figure 13 shows that this balance applies also to our model since a large portion of the deep equatorward flow is returned poleward in the upper ocean, that is, in the WBC, in the model's North Atlantic overturning and in the South Pacific in the more diffusive runs. The other possible configurations with two or more counter-rotating cells that occur when the Sverdrup flow and the bottom water flow are in opposite directions are found in the South Atlantic and the North Pacific. These configurations are obviously less efficient at transporting heat given that the different cells transport heat in opposite directions.

6. Discussion and conclusions

Our analysis sheds light on how the background diffusivity, and indeed turbulent diffusivity in general, affects the ocean general circulation and its associated

Brought to you by NOAA Central Library | Unauthenticated | Downloaded 08/28/24 07:12 PM UTC

meridional heat transport. The background diffusivity affects the diffusivity most strongly in the lower thermocline, where other parameterizations contribute little to the vertical diffusivity. Somewhat paradoxically, an increase of the background diffusivity from the very small reference value leads to decreased diffusivity below 2000 m, as an indirect effect of stronger stratification at these depths. The result of the combined changes in diffusivity and stratification is that the average vertical diffusive buoyancy transport κN^2 increases almost uniformly below 500 m as the background diffusivity increases.

The climatic impacts of our diffusivity changes are substantial; the volume-mean ocean temperature differs by 3.6°C between the least and the most diffusive runs, the SST by 2.4°C, and global-mean 2-m air temperature by 3°C. Although it is difficult to pin down a single reason for why the diffusivity changes cause these large climatic changes, we believe that the most important effect is the diffusivity-driven increase in the meridional overturning and associated heat transport. This increase is nearly compensated by a decrease of the atmospheric heat transport, but nevertheless brings about a near vanishing of sea ice, especially around Antarctica, which in turn leads to a strong atmospheric warming at high southern latitudes, a reduced meridional temperature gradient, a decreasing zonal wind stress, and a weakened Ferrel cell. An interesting parallel can be drawn to the recent work of England et al. (2017) that probes the effects of closing Drake Passage in an AOGCM. Their perturbation is completely different to ours, and indeed so is the response of the ocean circulation. Yet, the effect of a sea ice reduction around Antarctica in their model seems to be very similar to that in ours. They also experience a strong atmospheric warming leading to a reduced meridional temperature gradient and weaker zonal winds. The Antarctic sea ice extent thus exhibits a strong, and robust, effect on climate, and further studies on its dependence of various climate parameters are therefore needed. It would, for example, be interesting to know if the Antarctic sea ice extent is more sensitive to MOC changes than its Arctic counterpart because of the more poleward position of the MOC maximum in the Southern Hemisphere as we speculate here. It should also be mentioned that, while both our study and that of England et al. (2017) probe the effects of a reduced Antarctic sea ice cover, an increasing ice cover is also thought to have large climatic impacts (Ferrari et al. 2014).

We also studied the ocean overturning circulation, which is often thought to be closely related to the meridional heat transport. The most robust result was found using the mixing energy $\left(\int \kappa N^2 dV\right)$ as the scaling parameter, as suggested by Saenko (2006). Both the upper and lower cells scaled reasonably close to $\Psi \propto (\kappa N^2)^{1/2}$, where κ and N^2 are the average values at the depths where the cells exist. However, more testing is needed to see whether this empirical result is true also for other perturbations and models. Our simulations also verify the hypothesis that the overturning maxima in the lower cell should coincide with the peak incrop area, put forth by de Lavergne et al. (2016). In fact, the large range of diffusivities probed here in equilibrium simulations probably give the strongest support yet for the generality of that conjecture.

To investigate the relation between overturning circulation and meridional heat flux, we computed the heat flux at the latitudes 20°N and 20°S in the various overturning cells separately for the Atlantic and the Indo-Pacific Oceans. The dominating contribution to the heat flux comes from the large overturning cells in the North Atlantic and the South Pacific. In these basins, the deep transport and the Sverdrup transport are both equatorward, and a substantial part of the poleward return flow occurs in warm western boundary currents.

The heat transport in the North Atlantic increases roughly proportionally to the overturning strength as the background diffusivity is increased. However, this is counteracted by a decrease of the northward heat transport in the Indo-Pacific subtropical cell, although the volume transport in that cell increases. The result is a moderate increase of the total ocean heat transport at 20°N. The poleward heat transport in the Southern Hemisphere increases more than in the Northern Hemisphere, mostly because of increasing heat transport in the large Indo-Pacific cell. However, less than half of this increase is caused by an increase in the overturning strength. The most important reason is instead a closer connection between the lower and upper parts of the large cell. As the diffusivity and vertical transport increases, more of the incoming bottom water returns near the surface instead of in the deep ocean, increasing the temperature contrast between northward and southward flowing and thereby the heat transport.

We conclude that the increased background diffusivity leads to increased vertical diffusive transport and to increased meridional heat transport in the ocean. It also leads to stronger overturning, as measured in depth–density coordinates. However, the relation between the overturning strength and the meridional heat transport is in fact quite complex, and one cannot interpret the increased heat transport as a

Brought to you by NOAA Central Library | Unauthenticated | Downloaded 08/28/24 07:12 PM UTC

direct consequence of stronger overturning, as is sometimes done.

Acknowledgments. We thank Bonnie Samuels, who kept these simulations running for so very long. We also thank the three anonymous reviewers whose comments have led to many improvements of this work.

APPENDIX

Calculation of Atmospheric and Oceanic Energy Transports

The oceanic heat transport, both the advective and the diffusive part, is calculated online using built-in model diagnostics. The atmospheric energy transport is calculated by subtracting the oceanic meridional heat flux from the TOA net radiative flux integrated southward of the latitude considered following the budget,

$$\frac{dE}{dT} = 0 = F_{\mathrm{TOA}} - F_O - F_A, \tag{A1}$$

where dE/dt is the time rate of change of energy in the atmosphere and ocean integrated southward of a given latitude, F_{TOA} is the net incoming radiation at the top of the atmosphere southward of the same latitude, and F_O (F_A) is the northward meridional energy transport at the given latitude in the ocean (atmosphere).

A small caveat exists with the advective oceanic heat transport. The oceanic meridional mass transport is generally not zero; rather, in a steady state, it equals the meridional water transport in the atmosphere, and this makes the result sensitive to the choice of reference temperature (Ferrari and Ferreira 2011). The advective oceanic heat transport is calculated using the model temperature in degrees Celsius as

$$H_T = \rho_0 c_p \int_x \int_z \upsilon T dx dz, \tag{A2}$$

where ρ_0 is a reference density, c_p is the specific heat capacity of seawater (assumed constant), and υ is the meridional velocity. If we then decompose $\upsilon = \upsilon' + \overline{\upsilon}$, where $\overline{\upsilon}$ is the small mean velocity through the transect, υ' is the departure from the mean, and we use the same decomposition for T, (A2) can be written as

$$H_T = \rho_0 c_p \int_x \int_z \upsilon' T' dx dz + \rho_0 c_p \overline{\upsilon}\,\overline{T} \int_x \int_z dx dz. \tag{A3}$$

The first term in (A3) is independent of the reference temperature (i.e., it is the same whether T is given in kelvins or degrees Celsius), while the second term is not. However, the second term is small compared to the first term when degrees Celsius is used because $\overline{T}$ is then quite close to zero. The net meridional flow in the ocean is typically less than 1 Sv and $\overline{T}$ is typically less than 10°C, which makes the second term in (A3) about two orders of magnitude smaller than the first one, see also Jayne and Marotzke (2001) for a similar assessment. Filtering out this contribution due to the mean flow is also clearly physically motivated by the fact that the net heat transport in the coupled ocean–atmosphere system due to this net flow is very small, its transport of 1 Sv should be compared to the atmospheric overturning of about 100 Sv and the oceanic of around 20 Sv.

REFERENCES

Alford, M. H., J. A. MacKinnon, H. L. Simmons, and J. D. Nash, 2016: Near-inertial internal gravity waves in the ocean. *Annu. Rev. Mar. Sci.*, **8**, 95–123, https://doi.org/10.1146/annurev-marine-010814-015746.

Anderson, J. L., and Coauthors, 2004: The new GFDL global atmosphere and land model AM2-LM2: Evaluation with prescribed SST simulations. *J. Climate*, **17**, 4641–4673, https://doi.org/10.1175/JCLI-3223.1.

Boccaletti, G., R. Ferrari, A. Adcroft, D. Ferriera, and J. Marshall, 2005: The vertical structure of ocean heat transport. *Geophys. Res. Lett.*, **32**, L10603, https://doi.org/10.1029/2005GL022474.

Bryan, F., 1987: Parameter sensitivity of primitive equation ocean general circulation models. *J. Phys. Oceanogr.*, **17**, 970–985, https://doi.org/10.1175/1520-0485(1987)017<0970:PSOPEO>2.0.CO;2.

Bryan, K., and M. D. Cox, 1967: A numerical investigation of the oceanic general circulation. *Tellus*, **19**, 54–80, https://doi.org/10.3402/tellusa.v19i1.9761.

Dalan, F., H. P. Stone, I. V. Kamenkovich, and J. R. Scott, 2005: Sensitivity of the ocean's climate to diapycnal diffusivity in an EMIC. Part I: Equilibrium state. *J. Climate*, **18**, 2460–2481, https://doi.org/10.1175/JCLI3411.1.

de Lavergne, C., G. Madec, J. Le Sommer, A. J. G. Nurser, and A. C. N. Garabato, 2016: On the consumption of Antarctic Bottom Water in the abyssal ocean. *J. Phys. Oceanogr.*, **46**, 635–661, https://doi.org/10.1175/JPO-D-14-0201.1.

Den Toom, M., and H. A. Dijkstra, 2011: Scaling the strength of the meridional overturning with vertical diffusivity in an idealized global geometry. *Tellus*, **63A**, 354–370, https://doi.org/10.1111/j.1600-0870.2010.00496.x.

Dunne, J. P., and Coauthors, 2012: GFDL's ESM2 global coupled climate–carbon Earth system models. Part I: Physical formulation and baseline simulation characteristics. *J. Climate*, **25**, 6646–6665, https://doi.org/10.1175/JCLI-D-11-00560.1.

England, M. H., D. K. Hutchinson, A. Santoso, and W. P. Sijp, 2017: Ice–atmosphere feedbacks dominate the response of the climate system to Drake Passage closure. *J. Climate*, **30**, 5775–5790, https://doi.org/10.1175/JCLI-D-15-0554.1.

Ferrari, R., and D. Ferreira, 2011: What processes drive the ocean heat transport? *Ocean Modell.*, **38**, 171–186, https://doi.org/10.1016/j.ocemod.2011.02.013.

——, M. F. Jansen, J. F. Adkins, A. Burke, A. L. Stewart, and A. F. Thompson, 2014: Antarctic sea ice control on the ocean circulation

Brought to you by NOAA Central Library | Unauthenticated | Downloaded 08/28/24 07:12 PM UTC

in present and glacial climates. *Proc. Natl. Acad. Sci. USA*, **111**, 8753–8758, https://doi.org/10.1073/pnas.1323922111.

——, A. Mashayek, T. J. McDougall, M. Nikurashin, and J.- M. Campin, 2016: Turning ocean mixing upside down. *J. Phys. Oceanogr.*, **46**, 2239–2261, https://doi.org/10.1175/JPO-D-15-0244.1.

Gargett, A. E., and G. Holloway, 1984: Dissipation and diffusion by internal wave breaking. *J. Mar. Res.*, **42**, 15–27, https://doi.org/10.1357/002224084788506158.

Gent, P. R., and J. C. McWilliams, 1990: Isopycnal mixing in ocean circulation models. *J. Phys. Oceanogr.*, **20**, 150–155, https://doi.org/10.1175/1520-0485(1990)020<0150:IMIOCM>2.0.CO;2.

Hallberg, R., and A. Adcroft, 2009: Reconciling estimates of the free surface height in Lagrangian vertical coordinate ocean models with mode-split time stepping. *Ocean Modell.*, **29**, 15–26, https://doi.org/10.1016/j.ocemod.2009.02.008.

Harrison, M. J., and R. W. Hallberg, 2008: Pacific subtropical cell response to reduced equatorial dissipation. *J. Phys. Oceanogr.*, **38**, 1894–1912, https://doi.org/10.1175/2008JPO3708.1.

Held, I. M., 2001: The partitioning of the poleward energy transport between the tropical ocean and atmosphere. *J. Atmos. Sci.*, **58**, 943–948, https://doi.org/10.1175/1520-0469(2001)058<0943:TPOTPE>2.0.CO;2.

Hieronymus, M., and J. R. Carpenter, 2016: Energy and variance budgets of a diffusive staircase with implications for heat flux scaling. *J. Phys. Oceanogr.*, **46**, 2553–2569, https://doi.org/10.1175/JPO-D-15-0155.1.

Hogg, A. M., H. A. Dijkstra, and J. A. Saenz, 2013: The energetics of a collapsing meridional overturning circulation. *J. Phys. Oceanogr.*, **43**, 1512–1524, https://doi.org/10.1175/JPO-D-12-0212.1.

Ito, T., and J. Marshall, 2008: Control of lower-limb overturning circulation in the Southern Ocean by diapycnal mixing and mesoscale eddy transfer. *J. Phys. Oceanogr.*, **38**, 2832–2845, https://doi.org/10.1175/2008JPO3878.1.

Jackson, L., R. Hallberg, and S. Legg, 2008: A parameterization of shear driven turbulence for ocean climate models. *J. Phys. Oceanogr.*, **38**, 1033–1053, https://doi.org/10.1175/2007JPO3779.1.

Jayne, S. R., 2009: The impact of abyssal mixing parameterizations in an ocean general circulation model. *J. Phys. Oceanogr.*, **39**, 1756–1775, https://doi.org/10.1175/2009JPO4085.1.

——, and L. C. St. Laurent, 2001: Parameterizing tidal dissipation over rough topography. *Geophys. Res. Lett.*, **28**, 811–814, https://doi.org/10.1029/2000GL012044.

——, and J. Marotzke, 2001: The dynamics of ocean heat transport variability. *Rev. Geophys.*, **39**, 385–411, https://doi.org/10.1029/2000RG000084.

Jochum, M., 2009: Impact of latitudinal variations in vertical diffusivity on climate simulations. *J. Geophys. Res.*, **114**, C01010, https://doi.org/10.1029/2008JC005030.

Johns, W. E., and Coauthors, 2011: Continuous, array-based estimates of Atlantic Ocean heat transport at 26.5°N. *J. Climate*, **24**, 2429–2449, https://doi.org/10.1175/2010JCLI3997.1.

Ledwell, J. R., A. J. Watson, and C. S. Law, 1993: Evidence for slow mixing across the pycnocline from an open-ocean tracer-release experiment. *Nature*, **364**, 701–703, https://doi.org/10.1038/364701a0.

Legg, S., R. W. Hallberg, and J. B. Girton, 2006: Comparison of entrainment in overflows simulated by z-coordinate, isopycnal and non-hydrostatic models. *Ocean Modell.*, **11**, 69–97, https://doi.org/10.1016/j.ocemod.2004.11.006.

Lu, J., G. A. Vecchi, and T. Reichler, 2007: Expansion of the Hadley cell under global warming. *Geophys. Res. Lett.*, **34**, L06805, https://doi.org/10.1029/2006GL028443; Corrigendum, 34, L14808, https://doi.org/10.1029/2007GL030931.

Marshall, J., K. C. Armour, J. R. Scott, Y. Kostov, U. Hausmann, D. Ferreira, T. G. Shepherd, and C. M. Bitz, 2014: The ocean's role in polar climate change: asymmetric Arctic and Antarctic responses to greenhouse gas and ozone forcing. *Philos. Trans. Roy. Soc. London*, **372A**, 20130040, https://doi.org/10.1098/rsta.2013.0040.

Milly, P. C. D., and Coauthors, 2014: An enhanced model of land water and energy for global hydrologic and Earth-system studies. *J. Hydrometeor.*, **15**, 1739–1761, https://doi.org/10.1175/JHM-D-13-0162.1.

Msadek, R., W. E. Johns, S. G. Yeager, G. Danabasoglu, T. L. Delworth, and A. Rosati, 2013: The Atlantic meridional heat transport at 26.5°N and its relationship with the MOC in the RAPID array and the GFDL and NCAR coupled models. *J. Climate*, **26**, 4335–4356, https://doi.org/10.1175/JCLI-D-12-00081.1.

Munk, W., 1966: Abyssal recipes. *Deep-Sea Res. Oceanogr. Abstr.*, **13**, 707–730, https://doi.org/10.1016/0011-7471(66)90602-4.

——, and C. Wunsch, 1998: Abyssal recipes II: Energetics of tidal and wind mixing. *Deep-Sea Res. I*, **45**, 1977–2010, https://doi.org/10.1016/S0967-0637(98)00070-3.

Nikurashin, M., and G. Vallis, 2011: A theory of deep stratification and the overturning circulation in the ocean. *J. Phys. Oceanogr.*, **41**, 485–502, https://doi.org/10.1175/2010JPO4529.1.

——, and ——, 2012: A theory of the interhemispheric meridional overturning circulation and associated stratification. *J. Phys. Oceanogr.*, **42**, 1652–1667, https://doi.org/10.1175/JPO-D-11-0189.1.

Nilsson, J., G. Broström, and G. Walin, 2003: The thermohaline circulation and vertical mixing: Does weaker density stratification give stronger overturning? *J. Phys. Oceanogr.*, **33**, 2781–2795, https://doi.org/10.1175/1520-0485(2003)033<2781:TTCAVM>2.0.CO;2.

Nof, D., and A. M. de Bohr, 2004: From the Southern Ocean to the North Atlantic in the Ekman layer? *Bull. Amer. Meteor. Soc.*, **85**, 79–87, https://doi.org/10.1175/BAMS-85-1-79.

Nycander, J., 2011: Energy conversion, mixing energy, and neutral surfaces with a nonlinear equation of state. *J. Phys. Oceanogr.*, **41**, 28–41, https://doi.org/10.1175/2010JPO4250.1.

Oueslati, B., and G. Bellon, 2015: The double ITCZ bias in CMIP5 models: Interactions between SST, large-scale circulation and precipitation. *Climate Dyn.*, **44**, 585–607, https://doi.org/10.1007/s00382-015-2468-6.

Robinson, A., and H. Stommel, 1959: The oceanic thermocline and the associated thermohaline circulation. *Tellus*, **11**, 295–308, https://doi.org/10.3402/tellusa.v11i3.9317.

Rojas, M., 2013: Sensitivity of Southern Hemisphere circulation to LGM and 4xCO_2 climates. *Geophys. Res. Lett.*, **40**, 965–970, https://doi.org/10.1002/grl.50195.

Saenko, O. A., 2006: The effect of localized mixing on the ocean circulation and time-dependent climate change. *J. Phys. Oceanogr.*, **36**, 140–160, https://doi.org/10.1175/JPO2839.1.

Samelson, R. M., and G. K. Vallis, 1997: Large-scale circulation with small diapycnal diffusion: The two-thermocline limit. *J. Mar. Res.*, **55**, 223–275, https://doi.org/10.1357/0022240973224382.

Simmons, H. L., S. R. Jayne, L. C. St. Laurent, and A. J. Weaver, 2004: Tidally driven mixing in a numerical model of the ocean general circulation. *Ocean. Modell.*, **6**, 254–263, https://doi.org/10.1016/S1463-5003(03)00011-8.

Brought to you by NOAA Central Library | Unauthenticated | Downloaded 08/28/24 07:12 PM UTC

St. Laurent, L. C., H. L. Simmons, and S. R. Jayne, 2002: Estimating tidally driven mixing in the deep ocean. *Geophys. Res. Lett.*, **29**, 2106, https://doi.org/10.1029/2002GL015633.

Stone, P. H., 1978: Constraints on dynamical transports of energy on a spherical plant. *Dyn. Atmos. Oceans*, **2**, 123–139, https://doi.org/10.1016/0377-0265(78)90006-4.

Toggweiler, J. R., and B. Samuels, 1998: On the ocean's large-scale circulation in the limit off no vertical mixing. *J. Phys. Oceanogr.*, **28**, 1832–1852, https://doi.org/10.1175/1520-0485(1998)028<1832:OTOSLS>2.0.CO;2.

Vallis, G. K., and R. Farneti, 2009: Meridional energy transport in a coupled atmosphere–ocean system: Scaling and numerical experiments. *Quart. J. Roy. Meteor. Soc.*, **135**, 1643–1660, https://doi.org/10.1002/qj.498.

Winton, M., 2000: A reformulated three-layer sea ice model. *J. Atmos. Oceanic Technol.*, **17**, 525–532, https://doi.org/10.1175/1520-0426(2000)017<0525:ARTLSI>2.0.CO;2.

——, A. Adcroft, S. M. Griffies, R. W. Hallberg, L. W. Horowitz, and R. J. Stouffer, 2013: Influence of ocean and atmosphere components on simulated climate sensitivities. *J. Climate*, **26**, 231–245, https://doi.org/10.1175/JCLI-D-12-00121.1.

Wunsch, C., and R. Ferrari, 2004: Vertical mixing, energy, and the general circulation of the ocean. *Annu. Rev. Fluid Mech.*, **36**, 281–314, https://doi.org/10.1146/annurev.fluid.36.050802.122121.

Zika, J. D., W. P. Sijp, and M. H. England, 2013: Vertical heat transport by the ocean circulation and the role of mechanical and haline forcing. *J. Phys. Oceanogr.*, **43**, 2095–2112, https://doi.org/10.1175/JPO-D-12-0179.1.

Brought to you by NOAA Central Library | Unauthenticated | Downloaded 08/28/24 07:12 PM UTC